Citation
Li, Z. and Yang, Q. and Fang, R. and Chen, W. and Hao, H. 2021. Origami metamaterial with two-stage programmable compressive strength under quasi-static loading. International Journal of Mechanical Sciences. 189: ARTN 105987.
http://doi.org/10.1016/j.ijmecsci.2020.105987

Origami metamaterial with two-stage programmable compressive strength under quasi-static loading

Zhejian Li[1], Qiusong Yang[2], Rui Fang[2], Wensu Chen[1]*, Hong Hao[1]*,

[1] *Centre for Infrastructural Monitoring and Protection, School of Civil and Mechanical Engineering, Curtin University, Australia*

[2] *School of Civil Engineering, Guangzhou University, China*

*Corresponding authors: wensu.chen@curtin.edu.au (W. Chen); hong.hao@curtin.edu.au (H. Hao)

Abstract

An origami metamaterial with two-stage programmable compressive strength is proposed by combining the stacked Miura-origami and rhombic honeycomb structure. By adjusting the geometries of the structure, the compressive response of each stage including the compressive strength and the densification strain can be programmed within a certain range. Furthermore, the initial peak force, as an undesired energy-absorbing characteristic, can be programmed to maintain at a low level. The commonly seen fluctuation of crushing resistance on honeycomb structure is also minimized during the second stage deformation. The crushing behaviour of origami metamaterial is investigated under quasi-static loading condition. The programmability of compressive properties is demonstrated for the two stages of the deformation. The analytical model of the two-stage compressive response of the proposed origami metamaterial is firstly developed with friction contribution being taking into consideration during the first deformation stage. The analytical model is then verified with numerical analysis and quasi-static compressive testing data. The programmability of its compressive properties such as the initial peak crushing resistance, mean crushing force for both stages of deformation are then analysed based on the verified analytical model.

Keywords: Origami metamaterial; two-stage compressive strength; programmable compressive properties; quasi-static loading

Nomenclature	
a, b	length of edges on the top section of the unit column
h_1, h_2	height of half a Miura-ori cell and height of a rhombic tube cell
$h_{1,0}$, $h_{1,f}$	the initial and final height of half a Miura-ori cell
H	overall height of the structure
W, L	width and length of the unit column
W_0, W_f	the initial and final width of the unit column
L_0, L_f	initial and final length of the unit column
m, n	number of unit column in X_1 and X_2 direction
x, y	number of Miura-ori cell and rhombic tube cell in the unit column
T	cell wall thickness
α	the angle of $A_2A_1B_1$ on the top section of the Miura-ori cell
β	the angle between two faces on the top section of the Miura-ori cell
θ	the angle between faces of Miura-ori cell and vertical plane
γ	the angle between faces of Miura-ori cell and rhombic tube cell
φ	the angle between faces of rhombic tube cell
A_{sweep}	the total swept area of bottom edges on base throughout crushing
μ	friction coefficient
P_{m1}, P_{m2}	mean crushing force of the structure during the 1st and 2nd stage of deformation with friction considered
F	crushing force of the unit column during the 1st stage of deformation without considering the friction resistance
F_{m1}	mean crushing force of the unit column during the 1st stage of deformation without considering the friction resistance
$F_{m1(m\times n)}$	mean crushing force of metamaterial with $m\times n$ unit column without considering the friction resistance
F_c	critical crushing force during the 1st stage of deformation
F_f	average friction force on bottom edges during the 1st stage of deformation
F_{mf}	mean friction contributed crushing force during the 1st stage of deformation
E_b	bending energy of the Miura-ori section of the unit column during the 1st stage of deformation
E_f	total friction energy from the interfaces during the 1st stage of deformation
$F_{m2,I}$, $F_{m2,II}$, $F_{m2,III}$	mean crushing force of each Type I, II, III element in rhombic honeycomb section during 2nd stage of deformation
M_0	plastic bending moment per unit length
σ_0	yield strength of the base material
κ	coefficient of effective crushing distance during 2nd stage of deformation
ρ_0	the density of the base material
ρ_r	relative density of the structure
ε_D, ε_{D1}, ε_{D2}	overall densification strain, densification strain of the 1st and 2nd stage of deformation

1 Introduction

Cellular structures including lattice, foam, honeycomb and corrugated structures, often consist of unit cells formed by a group of the interconnected plate, sheets or struts [1]. Due to the advantages such as lightweight and high strength to weight ratio, these structures have been widely used and extensively studied [2-8]. The mechanical properties of these cellular structures can be architected based on the parameters such as geometries of the unit cell and the relative density. For instance, the microstructure of foam and lattice material can be categorized into bending or stretching dominated structures depending on the typical deformation of cell walls and struts, where stretching dominated structures often have significantly higher compressive strength than the bending dominated structures [1, 4]. The mechanical properties of honeycomb and corrugated structure are also governed by the geometries of the unit cell [9, 10].

Mechanical metamaterials are defined as a class of multiscale structures, which exhibit characteristics of unusual deformation or counterintuitive mechanical responses [11], such as negative Poisson's ratio [12, 13], negative thermal expansion [1], multi-stability [14-16], programmable stiffness [17]., etc. The unique mechanical properties of the structures are generated mostly from the structuring of the unit element rather than the mechanical behaviour of the base material. For example, by arranging the struts and cell wall within each unit cell of a cellular structure, auxetic metamaterials with a negative Poisson's ratio could be achieved in 2D [18, 19] and 3D [20, 21], even though the base material possess a positive Poisson's ratio. Under compression, the auxetic material contracts in the direction perpendicular to the direction of compression, resulting in an enhanced energy absorption against impact loads [22-24].

Origami structures have received wide attention in the area of mechanical metamaterials, as sheet material can be transformed into complex geometrical structures through coordinated folding [17, 25, 26]. Geometries of origami mechanical metamaterial are governed by parameters such as the magnitude, quantity, sequence, location and direction of the folds [1]. Kinematics and mechanical properties of origami structures, especially Miura-type origami structures, have been extensively studied [27-32]. Origami based mechanical metamaterials were investigated as well due to the unique properties, such as negative Poisson's ratio and self-locking. Stacked Miura-ori metamaterials were investigated for their folding kinematics and energy absorption capacity [25, 26, 33]. Origami metamaterial with graded stiffness was proposed by varying the geometries on each stacked Miura-ori layer [34]. Origami-inspired deployable mechanical metamaterial with tunable stiffness was studied [35]. Miura-ori tubes assembled metamaterial with reconfigurable stiffness was proposed and investigated [36]. Origami mechanical metamaterial with programmable two-stage stiffness via self-interlocking was studied [17]. Recently, the studies on Miura-ori based mechanical metamaterials with multiple stages of deformation were carried out [37, 38]. By combining the Miura-ori and honeycomb structure, a graded effect can be achieved through a developable creased pattern and good energy absorption capability has been demonstrated [37]. The programmability of Poisson's ratio and stiffness was investigated for multi-stage origami mechanical metamaterials based on curved-crease Miura-ori [38]. However, the crushing responses such as peak and mean crushing force of the multi-stage origami metamaterial have not been investigated.

In this study, a two-stage mechanical origami metamaterial with programmable crushing behaviour is proposed. The proposed metamaterial is developed by combining Miura-ori with rhombic honeycomb structure. Due to the different deformation of the Miura-ori and rhombic honeycomb sections, a two-stage crushing response can be achieved. The compressive properties, such as compressive strength and densification strain for both stages, can be programmed by adjusting the geometric parameters, as shown in Figure 1. Initial peak force during the first stage can be minimized and the commonly seen fluctuation of the crushing resistance on honeycomb structure is also minimized during the second stage deformation.

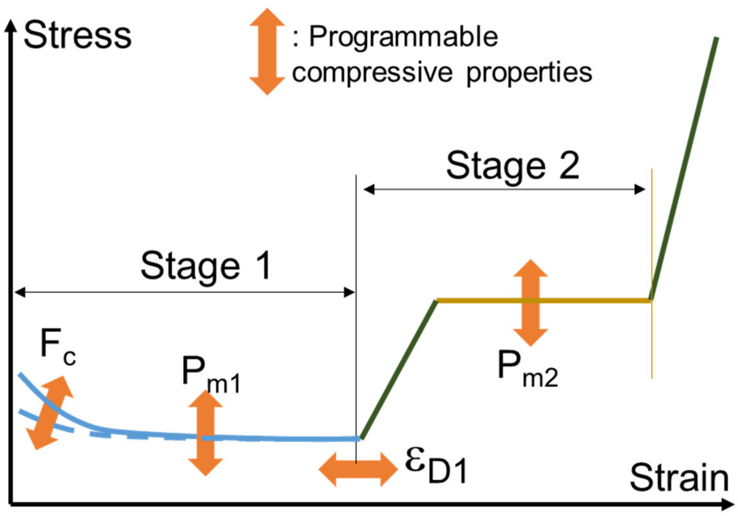

Figure 1. Illustration of the programmable compressive properties of the proposed origami metamaterial

The analytical model was firstly developed for the proposed structure to predict the mean crushing force and determine the initial peak force during the first stage deformation under quasi-static lateral crushing. Due to the equal and opposite Poisson's ratio in the two in-plane directions, the stacked Miura-ori section expands and contracts in both in-plane directions when subjected to the out-of-plane crushing, results in sliding of the edges at the contacting surface. The additional crushing resistance contributed by friction during this sliding was considered in the model. The analytical model was then verified against numerical simulations and crushing tests. The programmability of initial peak force, mean crushing force and densification strain against governing geometric parameters was analyzed using the validated analytical model.

2 Geometric parameters

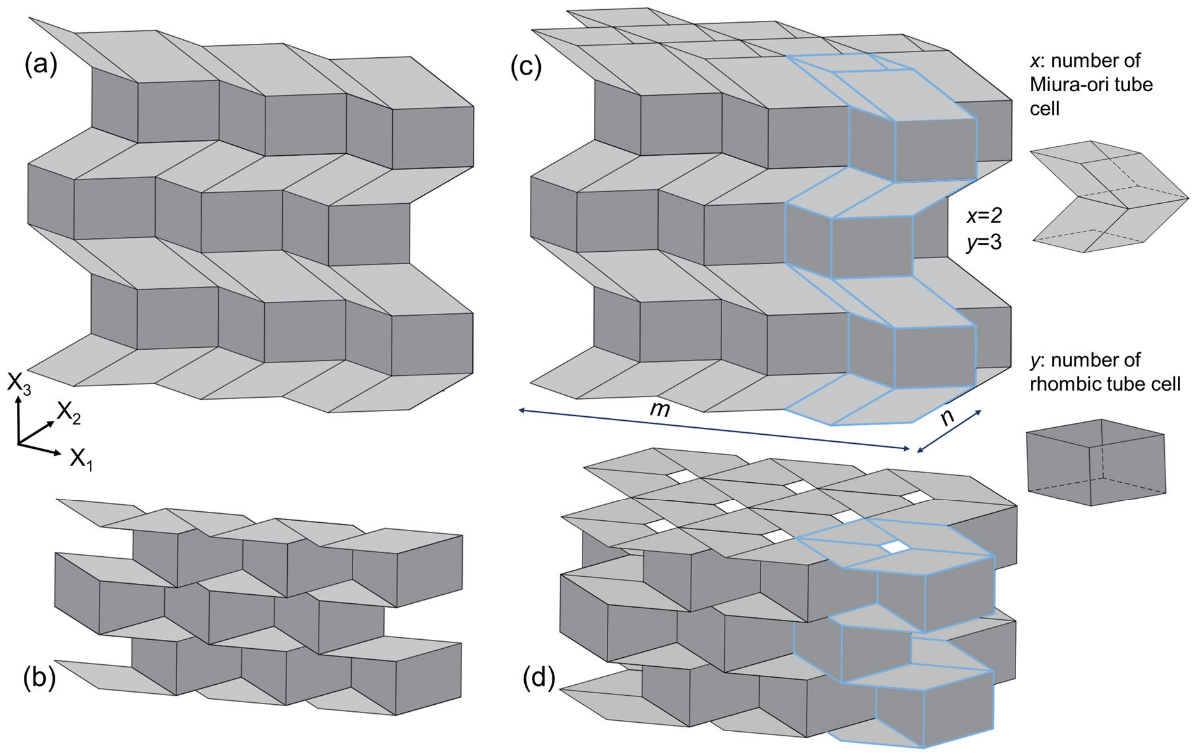

Figure 2. (a) Initial state and (b) end of the first stage deformation of single-sheet origami metamaterial; (c) initial state and (d) end of the first stage deformation of origami metamaterial with *m=3 n=2 x=2 y=3;* unit column is marked out in blue lines

The proposed origami metamaterial combines the Miura-origami with rhombic honeycomb structure. The Miura-type metamaterial is often referred to as the structure made of stacks of Miura-ori sheet layers, which have a series of tessellated zig-zag crease patterns on each layer. The stacked layers then form the Miura-type metamaterial with different compressive properties in the different principle directions and a changing Poisson's ratio throughout crushing [25]. The rhombic honeycomb structure has the profile of a parallelogram for each unit cell instead of a hexagon on the conventional honeycomb structure. Similar to honeycomb structure, rhombic honeycomb structure can provide high compressive resistance under out of plane crushing [39]. The proposed origami metamaterial that combines Miura-type metamaterial and rhombic honeycomb deforms in two stages under compression. The Miura-ori portion of the structure deforms first, followed by the deformation on rhombic honeycomb section.

The initial state and the end of the first stage deformation of the proposed structure are shown in Figure 2. During the first stage of deformation, the faces of the Miura-ori sections undergo bending deformation along the existing creases with minimal deformation on the faces, therefore generate relatively low yet uniform crushing resistance throughout the deformation [26]. Once the faces of Miura-ori sections flatten out, the layers of the honeycomb sections start to buckle and provide a higher crushing resistance during the second deformation stage.

In this study, origami metamaterial with two layers of Miura-ori cell (x=2) are divided and separated by three layers of the rhombic honeycomb (y=3) along X_3 direction throughout this paper. The metamaterial is divided into vertical “S-shaped” tubes with an array of $m \times n$ unit column in X_1 and X_2 directions, respectively. To analytically model the crushing response of the proposed two-stage metamaterial, a unit column including x number of Miura-ori tube cell and y number of rhombic tube cell is selected as marked out in blue lines in Figure 2. Geometric parameters are shown in Figure 3. The vertices are the intersection of the edges and marked as $A_{1\text{-}4}$, $B_{1\text{-}4}$, $C_{1\text{-}4}$, $D_{1\text{-}4}$ in Figure 3 (b) along the top, middle and bottom sections of the Miura-ori tube cell and rhombic tube cell. The pattern geometry is governed by six parameters only: the edge length of the top section, a, b; the angle of the top face, α; the folding angle between a top sidewall ($A_1B_1B_2A_2$) and vertical plane ($A_1B_1B_3A_3$), θ; the middle section height, h_2; and the sheet thickness, t. Other parameters can be determined as follows:

$$W = 2a \cdot \sin\theta \sin\alpha \tag{1}$$

$$h_1 = \frac{b \cdot \cos\theta \tan\alpha}{\sqrt{1+\cos^2\theta \tan^2\alpha}} \tag{2}$$

$$L = 2a\sqrt{1-\sin^2\theta \sin^2\alpha} \tag{3}$$

$$H = 2xh_1 + yh_2 \tag{4}$$

$$\sin\left(\frac{\varphi}{2}\right)=\sin\theta\sin\alpha \tag{5}$$

$$\sin\left(\gamma-\frac{\pi}{2}\right)=\frac{\cos\theta}{\cos\alpha\cdot\sqrt{1+\cos^2\theta\tan^2\alpha}} \tag{6}$$

$$\rho_r=\frac{8xab\sin\alpha\cdot t+4yah_2t}{W\cdot L\cdot(2xh_1+yh_2)} \tag{7}$$

where W and L are the width (A_2A_4) and length (A_1A_3) of the unit column, h_1 is the height of the half of a Miura cell; H is the overall height of a unit column, x, y is the number of Miura-ori cell and rhombic tube cell in a unit column, φ is the angle between the middle section faces ($B_2C_2C_3B_3$ and $B_3C_3C_4B_4$), and γ is the angle between adjacent faces of the top and middle sections ($A_1B_1B_2A_2$ and $B_1C_1C_2B_2$). ρ_r is the volumetric density.

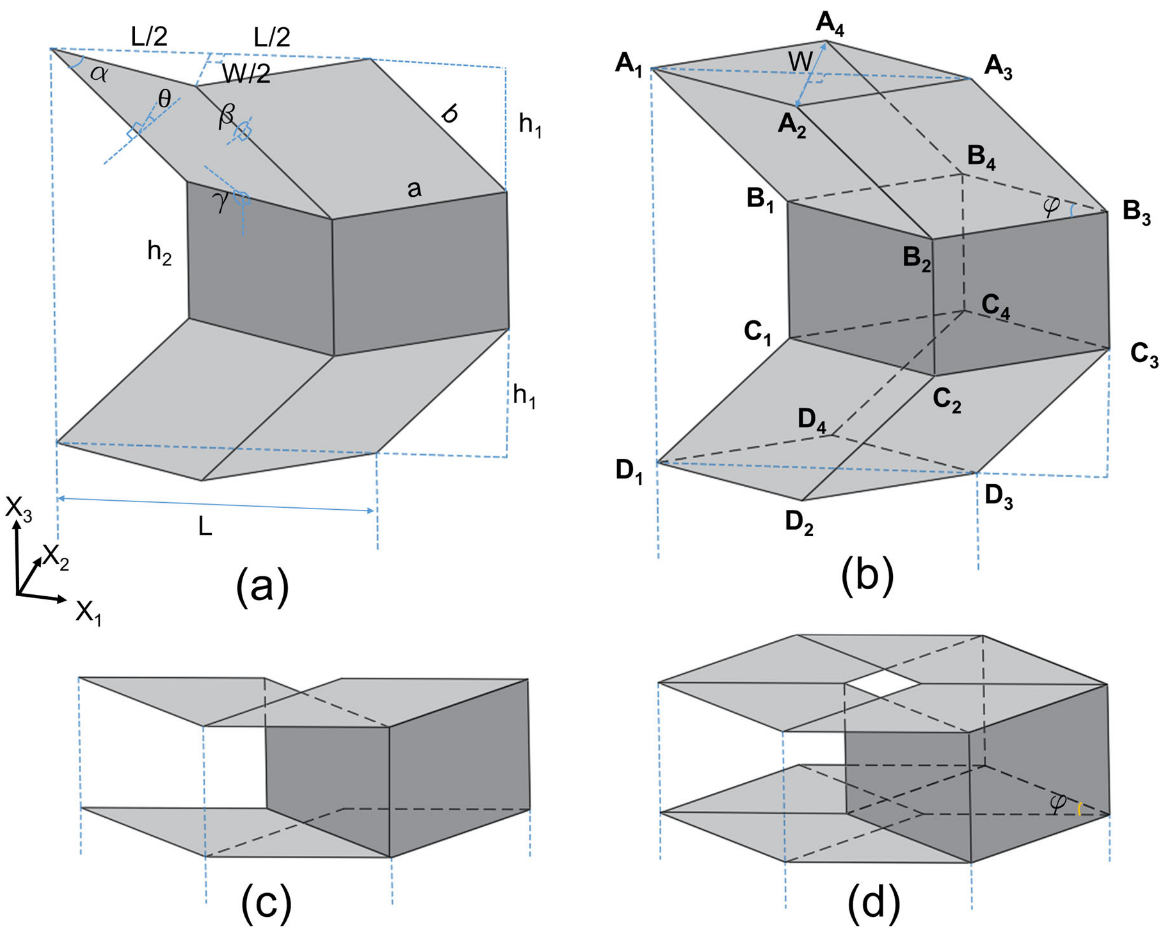

Figure 3. Geometric parameters at the initial state for (a) sheet; (b) column cell; and at the end of the first stage of deformation (c) sheet; (d) column cell

3 Analytical model

The analytical derivation of the crushing response of the proposed origami metamaterial can be divided into two parts owing to the two-stage deformation. Ductile metal sheet such as aluminium sheet is selected as the material for the proposed origami metamaterial, as it can undergo large plastic deformation and absorb energy. Furthermore, ductile metal sheet can be easily formed into desired shapes by press moulding. It is assumed that the strain hardening at the folding creases caused by press moulding fabrication is not considered and only plastic energy is considered during the compression of the proposed metamaterial.

3.1 1st stage of deformation

In this section, the first stage of deformation is modelled. Throughout the 1st stage crushing, the bending deformation along the existing folding creases such as A_1B_1, B_1B_2 and B_1C_1 is expected with minimal buckling deformation on the faces, as suggested by the previous studies [26, 33]. Thus, only bending along the existing folding creases are considered during the first stage of deformation. Friction induced additional compression force is considered in this study, as the contacting base area is constantly changing during the 1st stage of crushing.

3.1.1 Crushing force of each unit column

The crushing force of a unit column during the first stage deformation along X_3 direction, F, can be expressed by including the bending in three groups of creases as follows

$$F \cdot x \cdot 2dh_1 = x \cdot 16bM_0 d\theta + x \cdot 16aM_0 d\gamma + y \cdot 4h_2 M_0 d\varphi \tag{8}$$

where x, y is the number of Miura-ori unit cell and rhombic tube cell in each unit column and M_0 is the plastic bending moment per unit length [40] as expressed as

$$M_0 = \frac{\sigma_0 \cdot t^2}{4} \tag{9}$$

where σ_0 and t are the yield strength and thickness of the metal sheet, respectively. Furthermore, the crushing force can be rewritten with respect to θ based on equation (8):

$$F \cdot x \cdot 2\frac{\partial h_1}{\partial \theta} d\theta = x \cdot 16bM_0 d\theta + x \cdot 16aM_0 \frac{\partial \gamma}{\partial \theta} d\theta + y \cdot 4h_2 M_0 \frac{\partial \varphi}{\partial \theta} d\theta \tag{10}$$

where

$$\frac{\partial h_1}{\partial \theta} = b\frac{\sin\theta\tan\alpha}{\left(1+\cos^2\theta\tan^2\alpha\right)^{3/2}};$$
$$\frac{\partial \gamma}{\partial \theta} = \frac{\sin\theta\sec\alpha}{(1+\cos^2\theta\tan^2\alpha)^{3/2}\sqrt{1-\frac{\cos^2\theta\sec^2\alpha}{1+\cos^2\theta\tan^2\alpha}}}; \tag{11}$$
$$\frac{\partial \varphi}{\partial \theta} = \frac{2\cos\theta\sin\alpha}{\sqrt{1-\sin^2\theta\sin^2\alpha}}$$

are obtained from equation (1)- (6) and

$$F = 8M_0\left[\frac{\left(1+\cos^2\theta\tan^2\alpha\right)^{3/2}}{\sin\theta\tan\alpha} + \frac{a\sqrt{1+\cos^2\theta\tan^2\alpha}}{b\tan\alpha\sqrt{\cos^2\alpha\left(1+\cos^2\theta\tan^2\alpha\right)-\cos^2\theta}}\right] + 4M_0\frac{h_2}{b}\frac{y}{x}\frac{\cos\alpha\left(1+\cos^2\theta\tan^2\alpha\right)^{3/2}}{\tan\theta\sqrt{1-\sin^2\theta\sin^2\alpha}} \tag{12}$$

The critical crushing force or the initial peak force during the 1st stage of deformation, F_c, occurs at its initial position. Since only plastic deformation is considered, F_c, is therefore obtained by substituting $\theta=\theta_0$ into equation (12) and expressed as

$$F_c = 8M_0\left[\frac{\left(1+\cos^2\theta_0\tan^2\alpha\right)^{3/2}}{\sin\theta_0\tan\alpha} + \frac{a\sqrt{1+\cos^2\theta_0\tan^2\alpha}}{b\tan\alpha\sqrt{\cos^2\alpha\left(1+\cos^2\theta_0\tan^2\alpha\right)-\cos^2\theta_0}}\right] + 4M_0\frac{h_2}{b}\frac{y}{x}\frac{\cos\alpha\left(1+\cos^2\theta_0\tan^2\alpha\right)^{3/2}}{\tan\theta_0\sqrt{1-\sin^2\theta_0\sin^2\alpha}} \tag{13}$$

where θ_0 is the initial angle of θ .

The bending energy throughout the crushing is expressed from equation (8) as

$$\begin{aligned} E_b &= 2x\int_{h_{1,0}}^{h_{1,f}} F\cdot dh_1 = x\int_{\gamma_0}^{\gamma_f} 16a\cdot M_0\cdot d\gamma + x\int_{\theta_0}^{\theta_f} 16b\cdot M_0\cdot d\theta + y\int_{\varphi_0}^{\varphi_f} 4h_2M_0 d\varphi \\ &= [16xa(\gamma_0-\gamma_f)+16xb(\theta_f-\theta_0)+4yh_2(\varphi_f-\varphi_0)]M_0 \end{aligned} \tag{14}$$

The mean crushing force without friction, F_{m1}, is obtained by substituting equation (2):

$$F_{m1} = \frac{E_b}{2x(h_{1,0}-h_{1,f})} = \frac{\left[8xa(\gamma_0-\gamma_f)+8xb(\theta_f-\theta_0)+2y(\varphi_f-\varphi_0)h_2\right]M_0}{xb\left[\frac{\cos\theta_0\cdot\tan\alpha}{(1+\cos^2\theta_0\cdot\tan^2\alpha)^{1/2}} - \frac{\cos\theta_f\cdot\tan\alpha}{(1+\cos^2\theta_f\cdot\tan^2\alpha)^{1/2}}\right]} \tag{15}$$

where γ_0 , θ_0 and γ_f , θ_f are the initial and final angles of γ and θ during the 1st stage deformation. The after-crush angle of θ_f can be calculated by assuming that the full densification of Miura-ori section is reached at the end of stage 1 compression [26], the volume consisting of eight faces on Miura-ori section becomes the same as the final volume of the Miura-ori section in a unit column:

$$16 \cdot \frac{1}{2} ab \sin\alpha \cdot t = W_f \cdot L_f \cdot 2h_{1,f} \tag{16}$$

and the after-crush angle of θ_f, γ_f are obtained as

$$\theta_f = \arccos\left(\sqrt{\frac{1}{2} - \sqrt{\frac{1}{4} - \frac{t^2}{a^2 \sin^2\alpha}}}\right) \tag{17}$$

$$\gamma_f = \frac{\pi}{2} + \arcsin\frac{\cos\theta_f}{\cos\alpha \cdot \sqrt{1 + \cos^2\theta_f \tan^2\alpha}} \tag{18}$$

where both θ_f, γ_f are close to but not equal to 90° due to column wall thickness.

The densification strain of the first stage of deformation, ε_{D1} is expressed as

$$\varepsilon_{D1} = \frac{2x(h_{1,0} - h_{1,f})}{2xh_{1,0}} = 1 - \frac{\cos\theta_f \sqrt{1 + \cos^2\theta_0 \tan^2\alpha}}{\cos\theta_0 \sqrt{1 + \cos^2\theta_f \tan^2\alpha}} \tag{19}$$

3.1.2 Mean crushing force of a structure with $m \times n$ unit columns

The crushing force with respect to angle θ of a unit column, as well as its mean crushing force are derived in the section 3.1.1. The mean crushing force of a structure with $m \times n$ unit columns is greater than the mean crushing force of the single unit column times $m \times n$ because of the strong bonding along the four longitudinal edges between the adjacent unit columns. It was reported that the additional bending energy due to bonding between adjacent cells is equal to the bending energy of the edge in the cell [6]. For example, the additional bending energy due to bonding connection with the adjacent unit cells along A_1B_1 is $2bM_0 d\theta$, equals to the bending energy of the edge A_1B_1 itself. Therefore, the overall crushing force of an $m \times n$ origami metamaterial, $F_{m1(m \times n)}$, can be written as:

$$F_{m1(m\times n)} = \frac{mn \cdot E_b}{2x(h_{1,0} - h_{1,f})} + \frac{[(m-1)n + (n-1)m] \cdot \left[2xb(2\theta_f - 2\theta_0) + y(\varphi_f - \varphi_0)h_2\right] M_0}{2x(h_{1,0} - h_{1,f})} \tag{20}$$

where the first term is related to the $m \times n$ individual unit columns and the second term is the number of bonding connections $(m-1)n + (n-1)m$, multiplied by the bending energy along each longitudinal bonding connection. Bending energy during the first stage deformation of a unit column, E_b, is given in equation (14).

3.1.3 Additional crushing resistance contributed by friction

The additional crushing resistance contributed by friction is considered in this section. During the first stage of compression, contacting edges of the structure on both top and bottom interfaces move along the two in-plane directions. Due to friction between the pressing surfaces and the top/ bottom edges, this sliding movement of the contacting top and bottom edges results in additional work done which is proportional to the swept area of the edges on the contacting surfaces throughout the first stage of deformation. An example of a structure with 3×2 unit columns is shown in Figure 4, under lateral compression, where the proposed origami metamaterial expands in X_2 direction and contracts in X_1 direction.

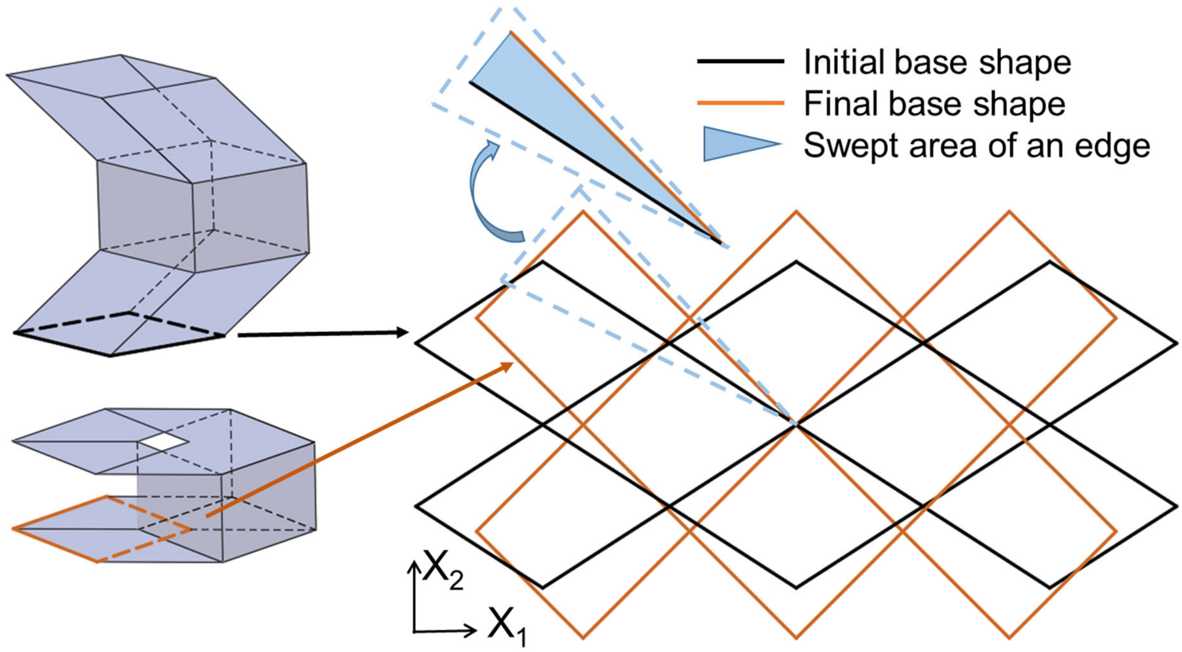

Figure 4. Illustration of the initial, final base shape and the swept area of an edge at the contacting surface on a structure with 3×2 unit columns

The work done due to the friction can be expressed as

$$E_f = \frac{2F_f}{4a \cdot mn} \cdot A_{sweep} = \frac{\mu F_{m1(m \times n)}}{2amn} \cdot A_{sweep} \tag{21}$$

where F_f is the average friction force on contacting edges of the whole structure during the first stage of deformation, μ is the friction coefficient, and A_{sweep} is the swept area of edges on contacting surfaces during the first stage of deformation, *m, n* are the number of unit column along the two in-plane directions. The friction force is assumed to be evenly distributed on the contacting edges over the total length of $4a \cdot mn$. It should be noted that a generic formula for swept area, A_{sweep} , of any given $m \times n$ structure is difficult to derive, and the swept area is measured in AutoCAD in this study. The compression force on the whole structure caused by friction, F_{mf}, is obtained by using work done by friction during the first stage of deformation divided by the compressed height as

$$F_{mf} = \frac{E_f}{2x(h_{1,0} - h_{1,f})} = \frac{\mu F_{m1(m\times n)} \cdot A_{sweep}}{4amnx(h_{1,0} - h_{1,f})} \tag{22}$$

and the contributing factor of friction is derived as

$$\frac{F_{mf}}{F_{m1(m\times n)}} = \frac{\mu \cdot A_{sweep}}{4amn \cdot x(h_{1,0} - h_{1,f})} \tag{23}$$

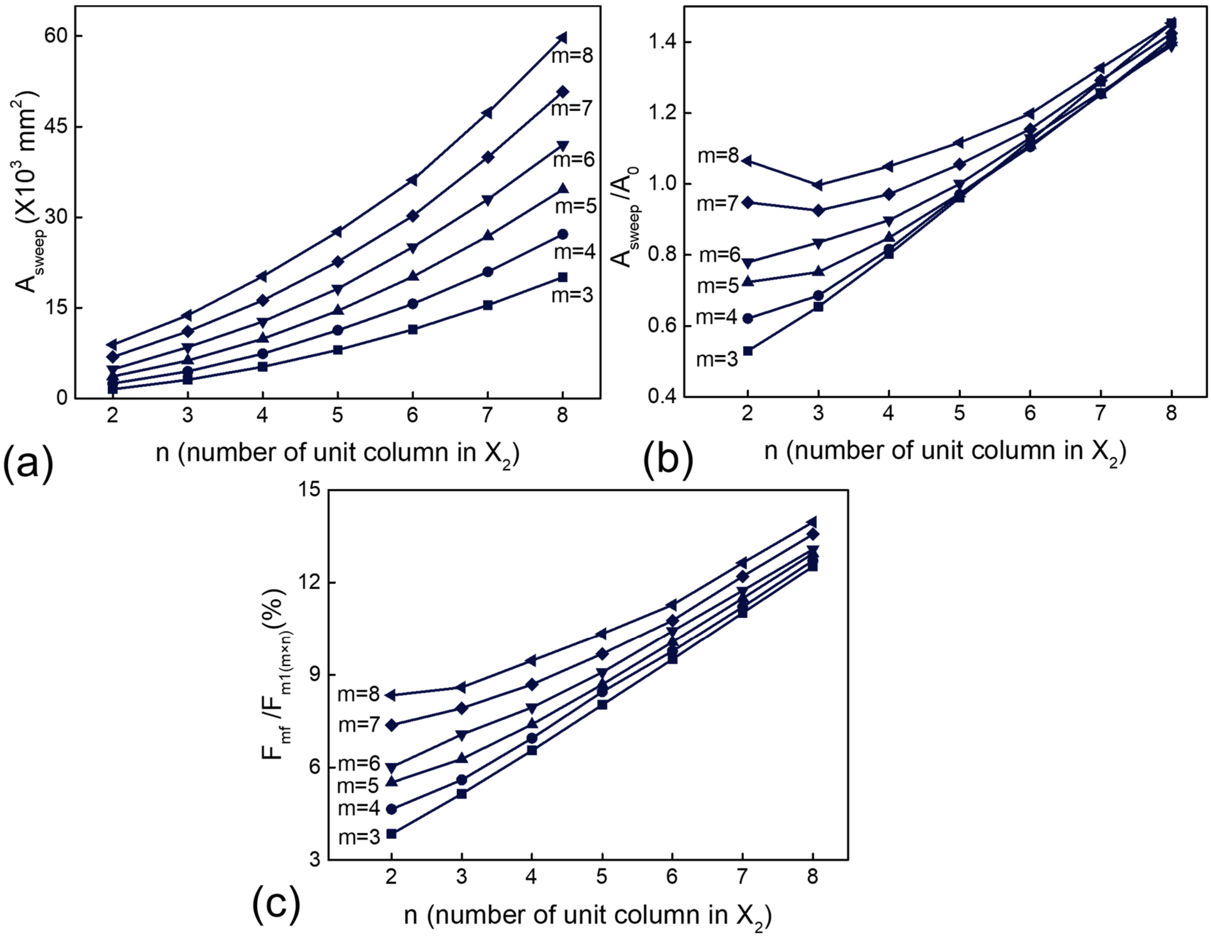

Figure 5. (a) Total swept area of interface edges after the first stage of crushing (A_{sweep}); (b) ratio of swept area (A_{sweep}) to initial base area (A_0); (c) ratio of friction contributed crushing force (F_{mf}) to the mean crushing force without considering friction ($F_{m1(m\times n)}$) during the first stage of deformation; with respect to the different number of the unit column (m, n); $a=b=20$ mm, $x=2$, $y=3$, $h_1=10.83$ mm, $\alpha=45°$, $\theta_0=50°$, $\mu=0.25$

The contribution factor increases with the number of unit column $m\times n$, due to the non-linear increase of bottom edge swept area with respect to the unit column number. Example of the influence of friction for the proposed structure with different array configurations is shown in

Figure 5. For the given pattern geometry, the friction contribution factor of mean crushing force increases from around 4% to 14%, when the number of unit column of the metamaterial increases from 3×2 to 8×8, because of the non-linear increase of the swept area at contacting surfaces.

The mean crushing force of the structure during the first deformation stage with friction contribution (F_{mf}) considered can be expressed as

$$P_{m1} = F_{m1(m\times n)} + F_{mf} = F_{m1(m\times n)}\left[1+\frac{\mu \cdot A_{sweep}}{4amnx(h_{1,0}-h_{1,f})}\right] \tag{24}$$

3.2 2nd stage of deformation

At the end of the first stage deformation, the Miura-ori section of the structure becomes fully crushed with a residual height of $2xh_{1,f}$ and this section is assumed to be densified. During the second stage of deformation, the buckling deformation of the faces of the rhombic honeycomb becomes dominate, resulting in a significantly higher crushing resistance than the first stage of deformation. Grid structures, including square and circular hollow columns [40-43], multi-cell columns [44-47], square and rhombic honeycomb have been extensively studied [7, 10, 39]. Analytical models with different coefficients of the crushing resistance of these structures were developed and compared. Therefore, an established analytical model for rhombic honeycomb is used for this study where inextensional damage mode was selected for corner element with an angle less than 135° [39, 45]. Three energy dissipation mechanisms were considered in this model, including the bending of the stationary hinge lines, the rolling of the moving hinge lines as well as the membrane deformation in the forming of the toroidal surface [6, 39].

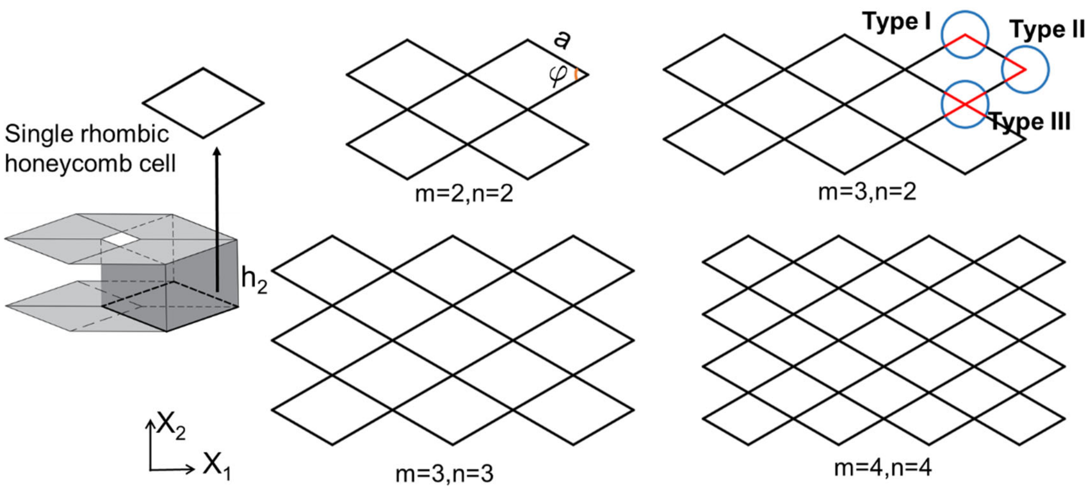

Figure 6. Rhombic honeycomb layer of origami metamaterial with different number of unit columns ($m \times n$)

The mean crushing force of rhombic honeycomb layer is calculated by summing up the mean crushing force of the two types of the corner elements and the 'X-shape' intersection elements, as shown in Figure 6. The mean crushing force for each Type I corner element, $F_{m2,I}$, [39] can be expressed as

$$F_{m2,I} = \frac{1}{2\varepsilon_{D2}}\sigma_0(\frac{a}{2})^{\frac{1}{3}}t^{\frac{5}{3}}\sqrt{\frac{2\pi\tan(\pi/2-\varphi/2)}{0.163\left[\tan(\pi/2-\varphi/2)+0.06/\tan(\pi/2-\varphi/2)\right]}} \tag{25}$$

and the mean crushing force for each Type II corner element, $F_{m2,II}$, [39] is expressed as

$$F_{m2,II} = \frac{1}{2\varepsilon_{D2}}\sigma_0(\frac{a}{2})^{\frac{1}{3}}t^{\frac{5}{3}}\sqrt{\frac{2\pi\tan(\varphi/2)}{0.163\left[\tan(\varphi/2)+0.06/\tan(\varphi/2)\right]}} \tag{26}$$

The mean crushing force for each Type III 'X-shape' intersection element, $F_{m2,III}$, [39] is predicted by

$$\begin{aligned} F_{m2,III} &= \frac{2}{\varepsilon_{D2}}\sigma_0(\frac{a}{2})^{\frac{1}{2}}t^{\frac{3}{2}}\sqrt{\pi\tan(\varphi/2)+4\pi\sec(\varphi/2)\left(\frac{2t}{b}\right)^{\frac{1}{2}}}\text{ ; for }\varphi\in(0,\pi/2] \\ F_{m2,III} &= \frac{2}{\varepsilon_{D2}}\sigma_0(\frac{a}{2})^{\frac{1}{2}}t^{\frac{3}{2}}\sqrt{\pi\tan(\pi/2-\varphi/2)+4\pi\sec(\pi/2-\varphi/2)\left(\frac{2t}{b}\right)^{\frac{1}{2}}}\text{ ; for }\varphi\in[\pi/2,\pi) \end{aligned} \tag{27}$$

where a is the edge length of the cell, t is the wall thickness, σ_0 is the yield strength of the base material, φ is the angle of the adjacent cell faces. It should be noted that the angle φ changes during the first stage of deformation, but remains unchanged during the second stage of deformation. φ used in this section can be obtained by substituting the final angle, θ_f, obtained from equation (17), into equation (5).

Densification strain of the second stage deformation, ε_{D2}, or the effective crushing coefficient referred in the previous studies [6, 39, 40], is the ratio of crushed distance and the original height of the rhombic honeycomb section. It was recorded to be 73% for a square tube under the inextensional mode of deformation [41], it can be also estimated from numerical results [39]. The rhombic honeycomb sections in the proposed structure are divided by the Miura-ori sections into multiple layers, resulting in a lower ratio of cell edge length to height than that of square tubes. This could lead to a lower effective crushing coefficient due to uncompleted folding after crushing. Thus, in this study, the effective crushing coefficient (ε_{D2}) is obtained from the numerical simulation rather than 73% of the conventional square tubes reported in [41].

The mean crushing force of origami metamaterial with 3×2 unit columns during the second stage P_{m2} is

$$P_{m2} = 2mF_{m2,I} + 2nF_{m2,II} + [(m-1)n + (n-1)m]F_{m2,III} \tag{28}$$

To summarize, the mean force of an $m \times n$ metamaterial without considering friction at interfaces can be calculated by using equation (20) for the displacement in X3 $\in (0, \varepsilon_{D1} 2xh_{1,0}]$ and equation (28) for the displacement in X3 $\in (\varepsilon_{D1} 2xh_{1,0}, \varepsilon_{D1} 2xh_{1,0} + \varepsilon_{D2} yh_2]$. Equation (24) can be used to calculate the 1st stage mean crushing force considering friction, where swept area, A_{sweep} needs to be measured for a specific $m \times n$ metamaterial. The overall densification strain can be expressed as

$$\varepsilon_D = \frac{\varepsilon_{D1} 2xh_{1,0} + \varepsilon_{D2} yh_2}{2xh_{1,0} + yh_2} \tag{29}$$

4 Model verification

4.1 Quasi-static crushing test

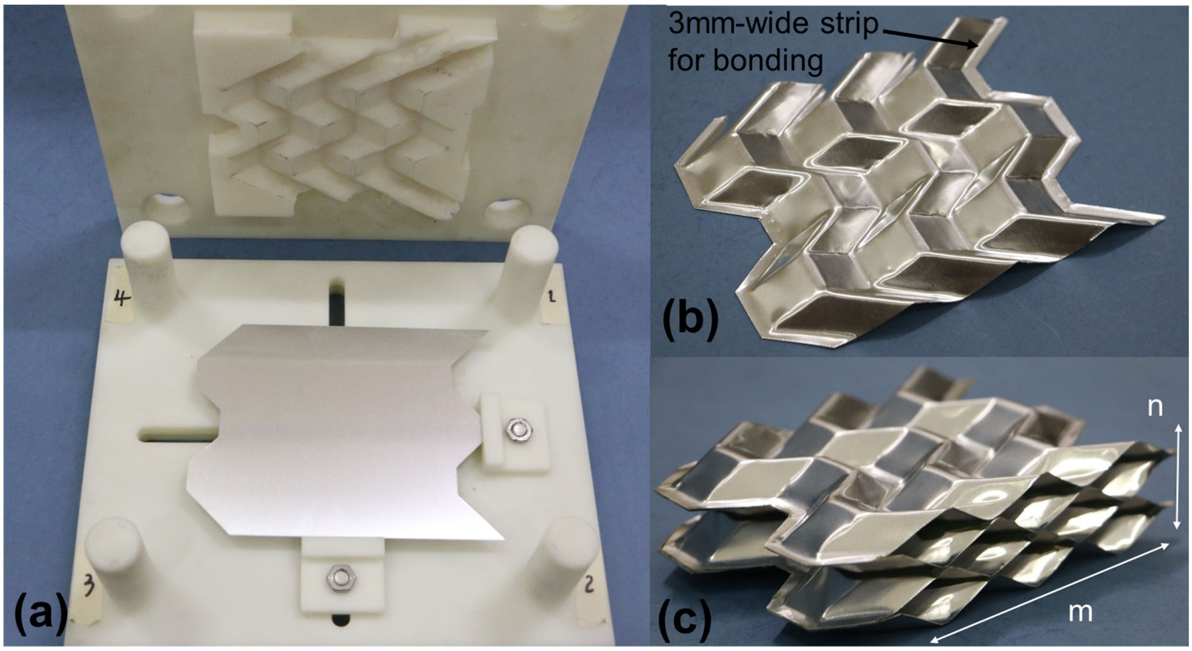

Figure 7. (a) 3D-printed pressing mould for layer fabrication; (b) pressed layer after trimming along the outer edges; (c) 3×2 specimen by bonding four heat-treated layers

Quasi-static crushing tests of 3×2 (m×n) origami metamaterials with and without heat treatment were carried out. The geometry parameters used for this metamaterials are given in Table 1.

To form the specimen with 3×2 unit columns, each layer was firstly fabricated by mould-pressing from Al 1060 metal sheet with a thickness of 0.26 mm, as shown in Figure 7 (a). The one-stage pressing mould was 3D printed using photopolymer. The pressed sheets were trimmed with a 3 mm-wide strip left on each end of the sheet for better gluing as shown in Figure 7 (b). Heat-treatment at 350°C for 4 minutes was applied to remove the residual stress caused in the mould pressing fabrication along the crease lines. As shown in Figure 7 (c), four heat-treated layers were then bonded together by using Ergo 1665 NB adhesive with tensile strength over 22 MPa and curing time of at least 24 hrs. SUNS® UT4304 universal testing machine was used for the quasi-static compression tests. The metamaterial specimens were placed between the cross-head and supporting disc without the constraint at interfaces. Both the supporting disc and cross-head have 150 mm diameter. The specimens were then crushed under quasi-static loading condition with a constant speed of 2 mm/min.

a (mm)	b (mm)	t (mm)	h_1 (mm)	h_2 (mm)	H (mm)	x	y	α	θ_0
20	20	0.26	10.8	15	88.3	2	3	45°	50°

Table 1. Geometric parameters for the metamaterial used in quasi-static tests

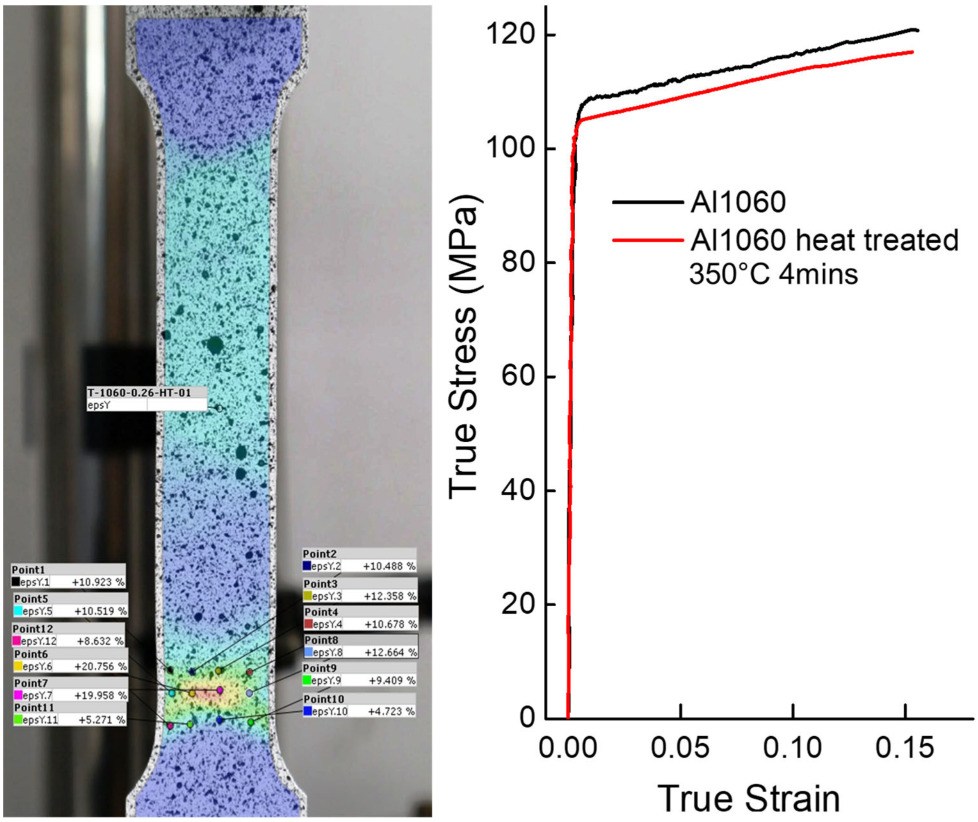

Figure 8. True tensile stress-strain curves of Al 1060 aluminium sheet with and without heat treatment, where the strain was measured using the 2D-DIC technique

The tensile tests were also carried out for the heat-treated and unheat-treated Al 1060 sheet used in the specimen preparation. The quasi-static loading rate was kept constant at 0.7 mm/min. The engineering stress-strain curves were firstly captured using 2-dimensional direct image correlation (DIC) technique and converted into true stress-strain curves, as shown in Figure 8. A slight reduction around 3 MPa was observed while Young's modulus remained the same. This reduction is caused by releasing a portion of the residual stress during heat treatment, as the sheet could be cold-rolled in the fabrication stage with work hardening. The density of Al 1060 is 2710 kg/m^3, and yield strength of Al 1060 is 110 MPa and 106 MPa, before and after 350°C heat treatment, respectively.

4.2 Finite element analysis

Numerical analysis of the tested specimens was conducted using FE software LS-DYNA. Piecewise linear plastic model was used for modelling the aluminium sheets of the 3×2 (m×n) origami metamaterials. The material properties measured including true stress-strain data for both cases were implemented in the material model. For simplicity, the bonding connections between the layers of the specimen were not included. Instead, the layers of pressed sheets were modelled as a whole structure. Mesh size of 1 mm was selected after the convergence tests. Both cross-head and support plate were modelled as rigid blocks. The friction between interfaces and within the structure was considered with a coefficient of 0.25 [48]. The crushing speed was set to be constant as 1m/s, which was found to be sufficient to simulate the quasi-static loading condition with the kinetic energy to internal energy less than 5% [48, 49].

4.3 Model validation

Load-displacement curves from experiments and FE analysis for different heat-treated conditions are firstly compared, as shown in Figure 9. The folding process induces residual stress via work hardening as the aluminium sheets are deformed plastically and lead to a higher material strength near the creases. This folding induced residual stress at the creases results in a higher crushing resistance of the 1st stage of deformation where most deformation occurs near the creases. Thus, higher crushing resistance during the 1st stage of deformation is observed in the test without heat treatment as compared to FE result, as marked out in blue and red solid lines in Figure 9 (b). The heat treatment was then carried out aiming to release the residual stress along the creases. The crushing resistance, especially the initial peak force, is reduced with 4 minutes of annealing, but the discrepancies can still be noticed during the 1st stage crushing as marked in blue and red dash lines, indicating residual stress near creases from mould-pressing is not fully released. However, further annealing leads to a noticeable drop in crushing resistance in the 2^{nd} stage. This is because the residual stress from metal sheet fabrication is released during the longer annealing process, besides of that from mould-pressing as intended. Therefore, a 4-minute heat treatment is used for the study despite the mould-pressing induced residual stress is not fully released. In other word, the crushing resistance during the 1^{st} stage of deformation from the test is expected to be higher than that of the analytical and FE results.

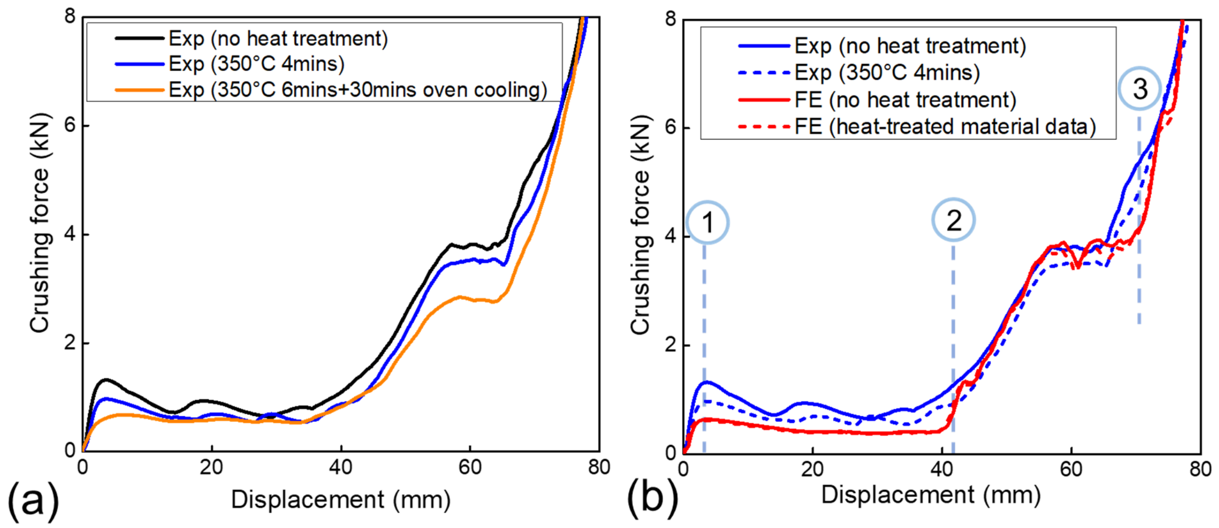

Figure 9. (a) Load-displacement curves from quasi-static crushing tests; (b) comparisons between FE and test data; with the initial state, end of the first and second stage deformation marked out as (1)/(2)/(3)

Three key states, i.e. initial, end of the 1^{st} and 2^{nd} stage of deformation from tests and FE results, corresponding to the three turning points in load-displacement curves (Figure 9 b) are compared in Figure 10. The deformation modes are matched between test and FE results, although the deformation mode in FE seems more ideal with minimal face deformation during the 1^{st} stage of deformation. It can be observed that the crease lines of the prepared specimens were not perfectly pressed with a noticeable bending radius around the designed lines, and slight imperfection was induced on the faces during the mould-pressing process. This imperfect folding leads to the slightly more face deformation in testing during the 1^{st} stage of deformation while only bending deformation along crease lines are observed from FE results. The face deformation also contributes to the slightly higher crushing resistance in tests than FE results. At the initial state of the 2^{nd} stage of deformation, the offsets between rhombic layers leads to a local buckling at the contacted areas rather than the multiple folding deformations common in honeycomb and tubular structure. Thus, no initial peak is observed during the 2^{nd} stage of deformation and it takes longer distance for the layer to reach plateau resistance. The offsets between rhombic honeycomb layers are governed by the geometric parameters of the Miura section, and there could be infinite number of possible values, where each offset between layers could affect the initial stage of deformation. Therefore, the limitation in analytical model at the initial stage during the deformation of rhombic honeycomb layer is noted.

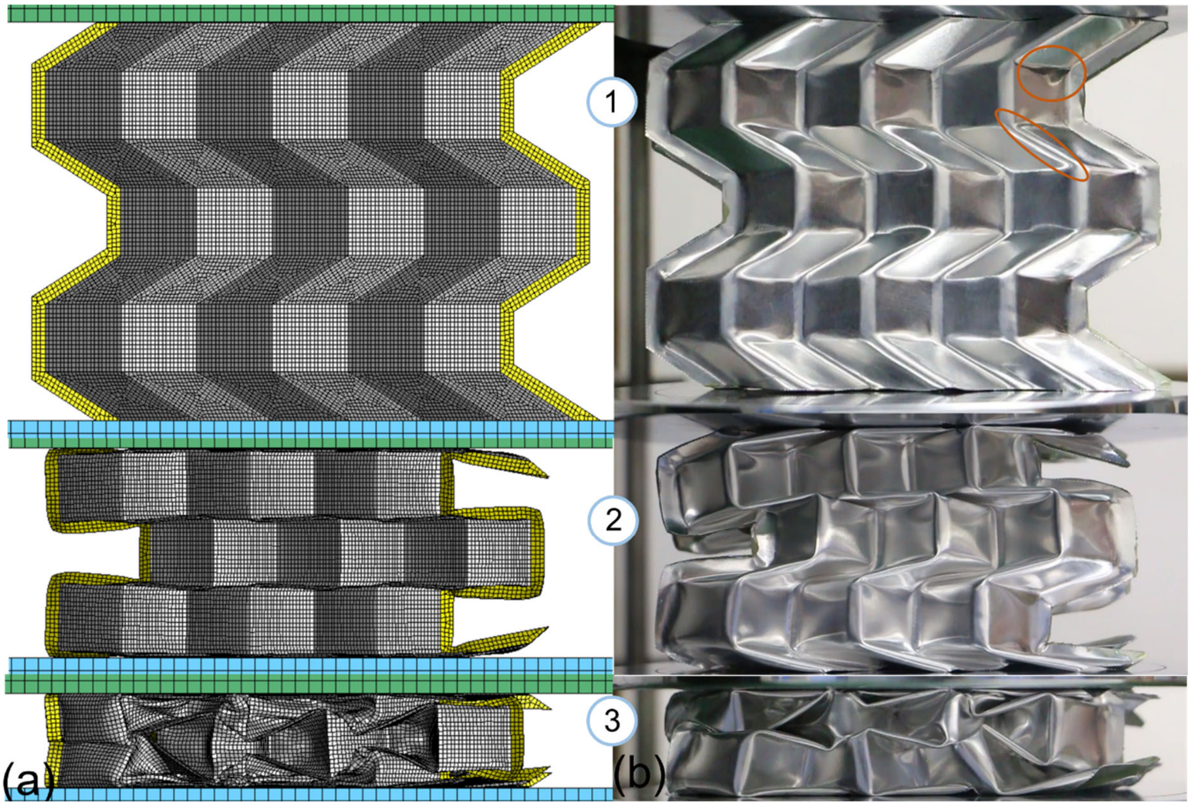

Figure 10. Deformation modes comparison between (a) FE result and (b) quasi-static test, at the initial stage (1), end of the first (2) and end of the second stage of deformation (3)

To better validate the analytical model, a numerical model without the strips which were used for bonding in the tests was then constructed based on the previously verified FE model, as shown in Figure 11. The analytical model for predicting the mean crushing forces of both stages of the metamaterial is compared with the numerical model without the bonding strips. The FE model without the strips shows a slightly lower crushing resistance and it is well matched with the analytical model of the mean crushing force prediction. The mean crushing forces of numerical results were taken average between initial, densification of the 1st and 2nd stage of deformation, as listed in Table 2. The mean crushing force P_{m1}, and densification strain, ε_{D1}, of the 1st stage of deformation are in good agreement with errors less than 7.5%, while the analytical mean crushing force of the 2nd stage, P_{m2}, is overestimated as compared to FE model. The overestimation is caused by the change of deformation mode at the initial stage of the 2nd

deformation stage. The analytical model of the 2nd stage mean crushing force is based on the classic kinematic model of the square tubes where the multiple folds are presented on the structures. For this proposed metamaterial, the rhombic honeycomb layers may not be stacked perfectly depending on the geometries and could lead to localized buckling deformation near the contacts at the beginning as shown in Figure 10. However, the overall trend and the mean crushing force at both deformation stages are in good agreement between FE and analytical model.

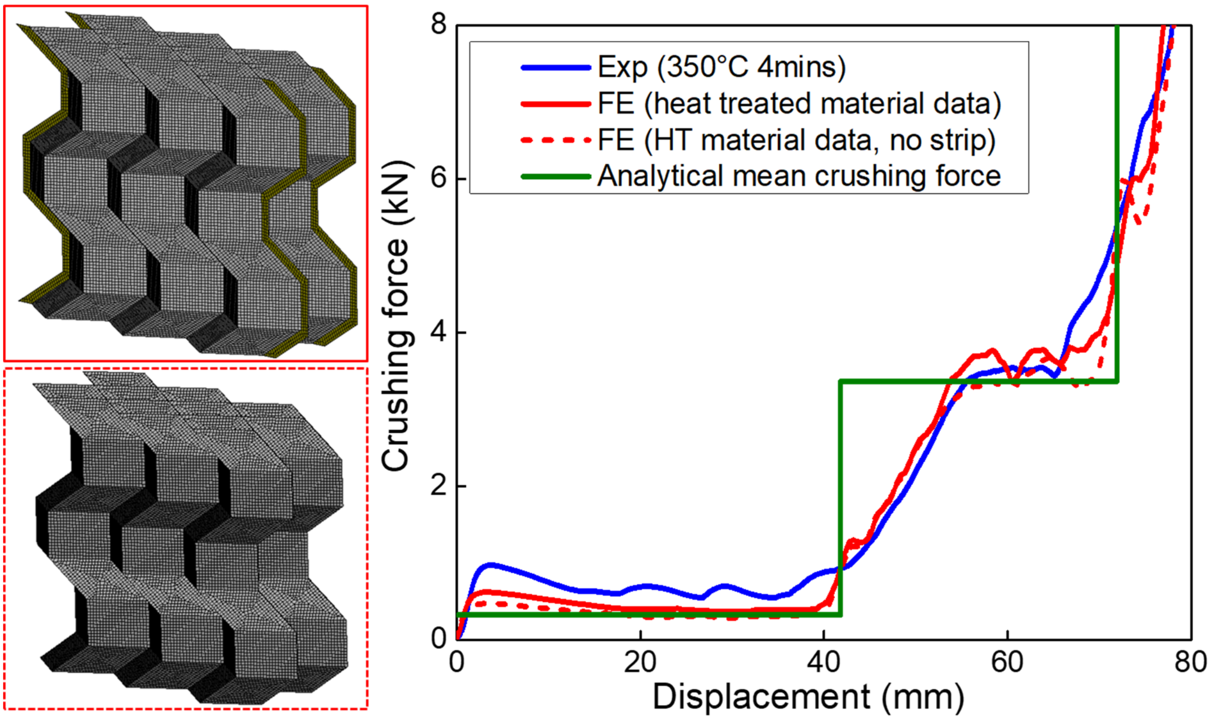

Figure 11. Load-displacement response comparison among test, FE and analytical model; Note: two FE models (with and without the 3mm strip) marked as solid and red dash lines are included to respectively represent the test and analytical model

P_{m1} (kN)			ε_{D1}			P_{m2} (kN)		
FE	Analytical	Error	FE	Analytical	Error	FE	Analytical	Error
0.347	0.321	-7.5%	0.933	0.965	3.4%	2.775	3.364	21.2%

Table 2. Mean crushing force comparison between analytical and numerical model without strip

5 Programmable compressive properties

5.1 Initial peak force

As an important criterion for energy absorbing structures, initial peak force must be kept below the threshold that would lead to damage or injury to the protected personnel and structures [50]. For common cellular structures such as honeycomb [10], lattice [51] and foam [52], both the initial peak force and mean crushing resistance are in power law relationship with the relative density. Therefore, the structure with a higher energy absorption capacity often has a high initial peak force. For the proposed origami metamaterial, the initial peak force could be significantly reduced with minimal reduction in mean crushing resistance by adjusting the related geometric parameters.

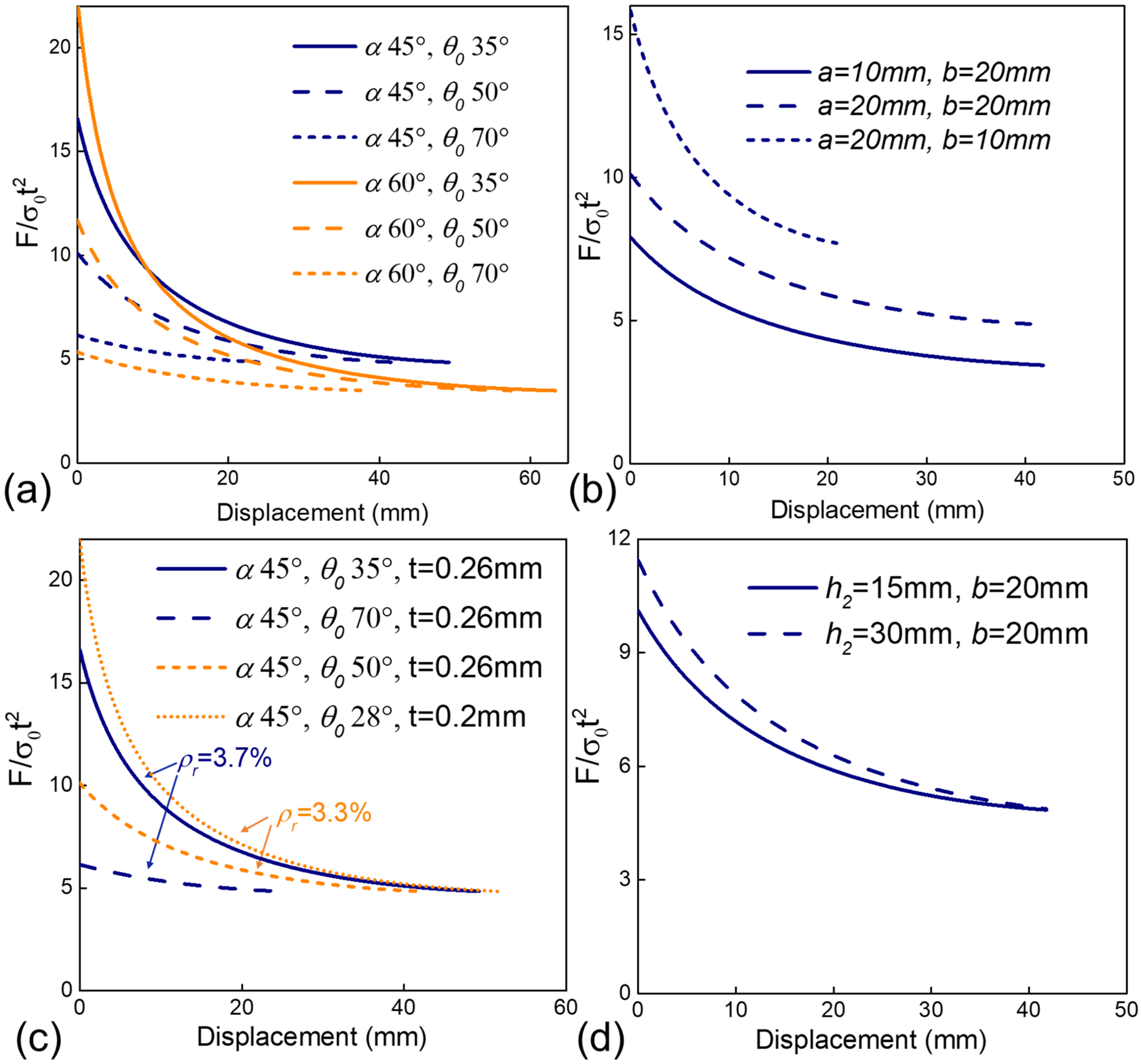

Figure 12. Comparison of normalized force-displacement curves of a unit column with different geometric parameters during the 1st deformation stage; (a) α and θ_0; (b) edge length

a, b; (c) relative density ρ_r ; (d) height of rhombic honeycomb layer, h_2; α=45°, θ_0=50°, a=b=20mm, h_2=15mm, t=0.26mm, x=2, y=3 unless otherwise noted;

The crushing responses of the 1st deformation stage of the proposed origami metamaterial with different geometric parameters are obtained from the analytical model of a unit column as shown in Figure 12. It should be noted that the unit column used for theoretical analysis is a unit cell of metamaterial rather than an actual column, as the metamaterial is very unlikely to be used in the form of a single column for energy absorption. Furthermore, friction contributed crushing force is not included as it is more prominent only for the structure with a large number of unit columns as shown previously in Figure 5 (c). Both face angle of the Miura-ori section α and the initial folding angle of θ_0 have significant influences on initial peak force, as shown in Figure 12 (a). With the increase in α and decrease θ_0, the initial peak force is reduced, where the crushing resistance at later stage is less affected. With the static angle α closer to 90°, the Miura-ori section is closer to a square tube. With a larger initial folding angle θ_0, the unit column becomes more slender and more difficult to bend along the horizontal creases. The crushable distance can be affected by these two angles as well. Furthermore, with the increase of edge length ratio of a/b, the initial peak force increases, while the crushable distance is solely dependent on b. Change of the layer height of rhombic honeycomb section, h_2, has minimal influence on the crushing response of the first stage of deformation, as the bending along vertical edges (h_2) of rhombic honeycomb section is minimal during the first deformation stage. It should be noted that the relative density, ρ_r , and wall thickness, t, different from common cellular structures, are not directly related to the initial peak force. For instance, as shown in Figure 12 (c), the origami metamaterial with lower volumetric density or wall thickness could have a larger initial peak force. The crushing response for the proposed origami metamaterial is predominately dependent on the governing geometric parameters a, b, α, and θ_0. In general, the trend of the crushing resistance as well as the initial peak force is strongly depended on α, and θ_0, and the mean crushing force is more affected by the side length a, b and wall thickness t.

The ratio of initial peak to average crushing resistance is often used to measure the efficiency of an energy absorbing structure. This ratio is calculated from analytical model for a unit column with various geometric parameters as given in Figure 13. Similar to Figure 12, a smaller static angle α, or a larger initial folding angle θ_0 leads to a smaller ratio of initial peak to average crushing resistance, indicating a more uniform crushing response and superior energy absorbing performance. The value of both edge length, *a, b* as well as the honeycomb layer height, h_2, have less influence on the peak to average ratio. The structures with the peak to average crushing force ratio less than 2 can be considered to be an ideal energy absorber, as this ratio could reach 3 or 4 for some square columns [45, 53].

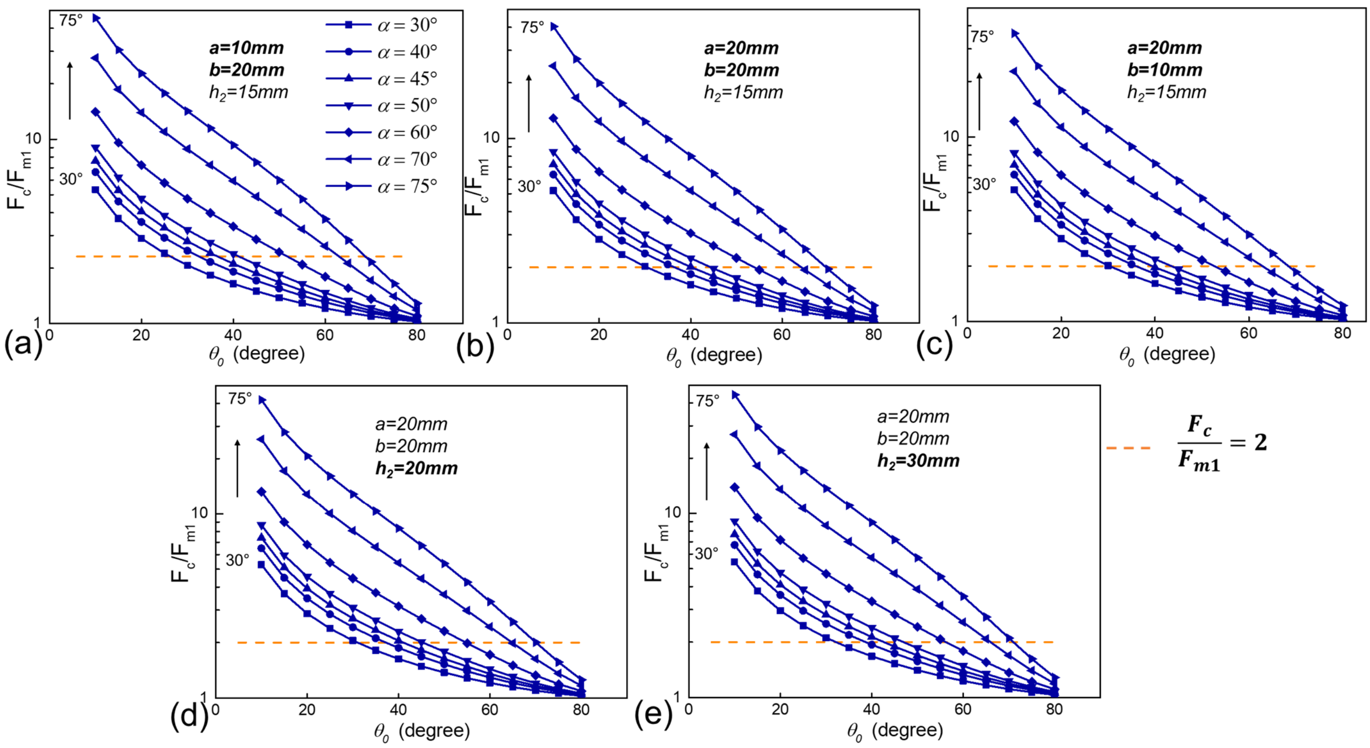

Figure 13. The ratio between initial peak (F_c) and average crushing force (F_{m1}) of a unit column during the 1st stage of deformation with respect to α, and θ_0 under different configurations; (a) *a*=10 mm, *b*=20 mm, h_2=15 mm; (b) *a*=20 mm, *b*=20 mm, h_2=15 mm; (c) *a*=20 mm, *b*=10 mm, h_2=15 mm; (d) *a*=20 mm, *b*=20 mm, h_2=20 mm; (e) *a*=20 mm, *b*=20 mm, h_2=30 mm;

5.2 Mean crushing force of the 1st and 2nd stages

The geometric parameters governing the mean crushing force of a unit column without the friction contribution during the 1st deformation stage are shown in Figure 14. It should be noted that only structures with uniform crushing response with peak to mean crushing force ratio less than 2 are included in Figure 14. The static angle, α, has the most significant influence on the mean crushing force during the 1st stage of deformation. The mean crushing force can be three times different with α changed from 75° to 30°, while little changes in mean crushing force can be observed with the change of θ_0, for all three edge length (*a,b*) configurations. A larger *a*/*b* may also lead to an increase in mean crushing force during the 1st stage of deformation. However, a smaller edge length of *b* leads to a reduction in crushable distance from equation

(2), while the densification strain of the 1st stage of deformation, ε_{D1}, is determined only by a, t, α, θ_0 according to equation (17) and (19). It should be noted that the connection bending resistance and the friction contributed crushing should be considered accordingly for the structures with multiple unit columns as expressed in equation (20) and (24)

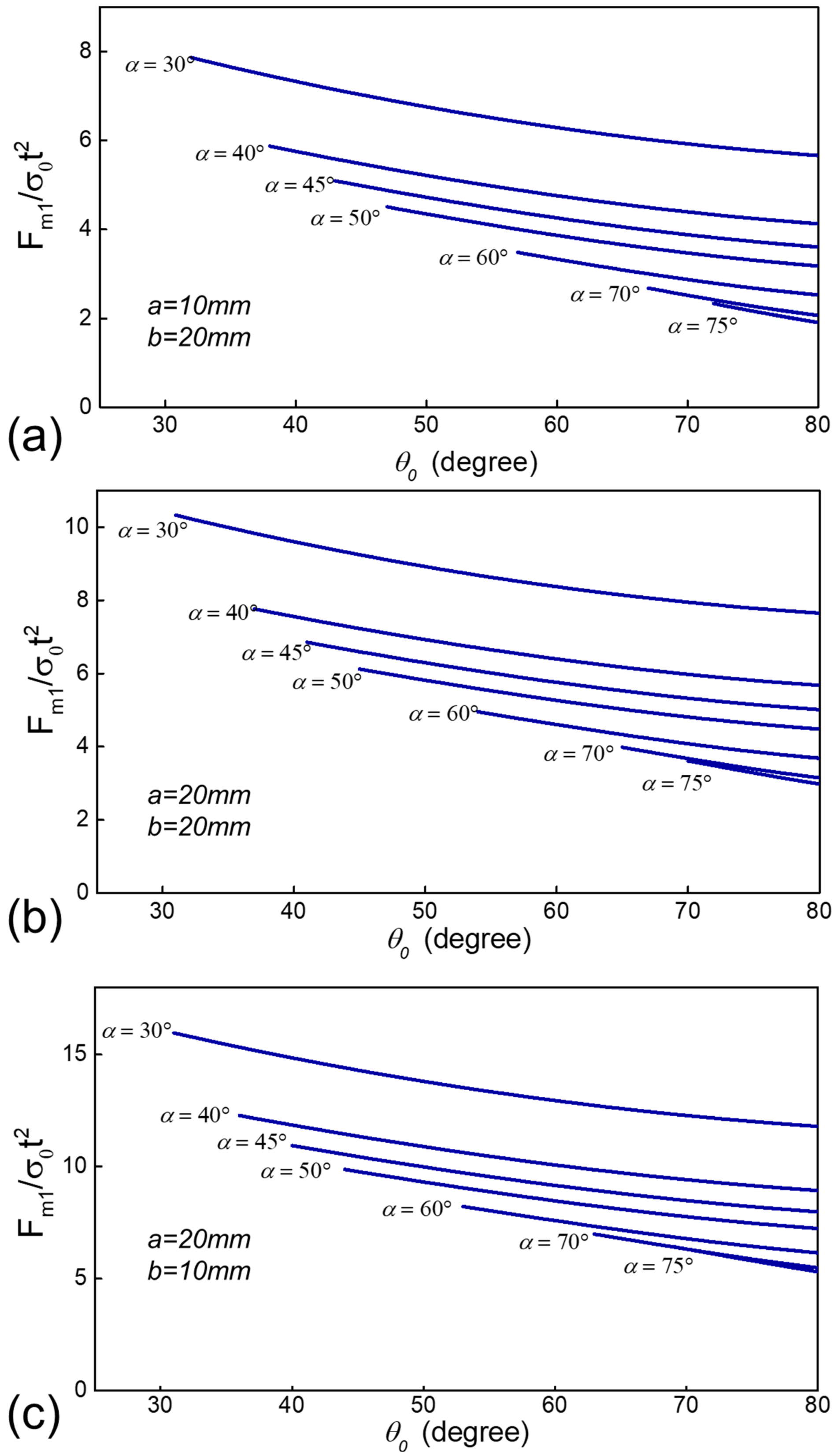

Figure 14. Mean crushing force of one unit column (F_{m1}) during the 1st deformation stage (without friction contribution) with respect to α, and θ_0 under different edge lengths; (a) a=10 mm, b=20 mm; (b) a=20 mm, b=20 mm; (c) a=20 mm, b=10 mm;

Similar to honeycomb and multi-corner structures, the mean crushing force of the proposed origami metamaterial during the 2nd stage of deformation is predominately dependent on the cell size and wall thickness. As shown in Figure 15, with the increase of cell wall angle φ until 90°, the mean crushing force increases slightly, due to the symmetry of the dominating factor of "X-shaped" intersection elements. For instance, an "X-shaped" intersection element with φ of 60° has the same mean crushing force as compared to that with φ of 120°, due to the symmetry of the element. Furthermore, the increase of the unit columns number (m×n) within a structure leads to a non-linear increase of the crushing force, due to the increase of the number of "X-shaped" elements, especially when m,n is small. It should be noted that the mean crushing force during the 2nd deformation stage is overestimated, as some localized buckling deformation occurs at the initial state of the 2nd stage deformation on the cell wall due to the off-set between rhombic layers. For the structures with $b=L_f$, the unit cells of rhombic honeycomb layer stack directly on top of the other as the offset distance is equal to the length of one unit cell at the beginning of the 2nd stage of deformation. The mean crushing force predicted by the analytical model is likely to be more accurate for such structure, as each unit cell on the rhombic honeycomb layer is supported by the lower layer.

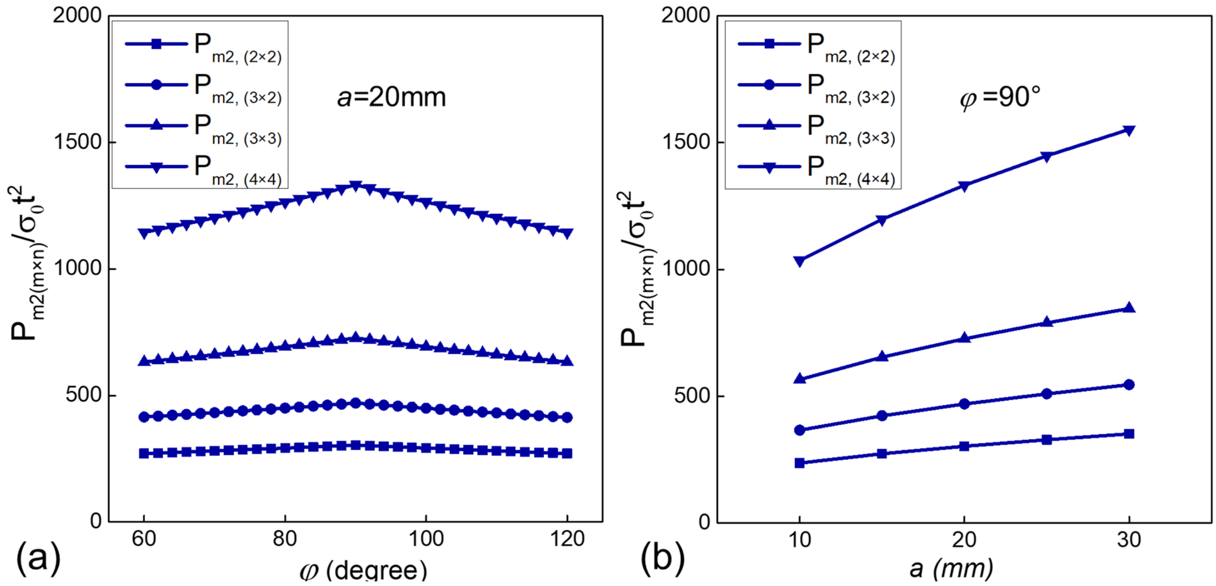

Figure 15. Mean crushing force of structure with $m\times n$ unit columns during the 2nd deformation stage ($P_{m2(m\times n)}$) with respect to different geometric parameters: (a) a=20 mm; (b) φ=90°; Note: h_2=15mm, t=0.26mm

6 Conclusions

By combining Miura origami and rhombic honeycomb structure, a two-stage origami metamaterial is proposed. The analytical model of the proposed structure has been developed to predict the compressive properties for both deformation stages. The additional crushing force contributed by friction due to the equal and opposite Poisson's ratio in two in-plane directions during the 1st stage of deformation is included in the analytical model. Numerical simulation and quasi-static crushing tests of heat-treated specimens have been carried out. The analytical model is then verified with the numerical and quasi-static testing results. Good agreement of compressive properties is obtained between the analytical and numerical model, with slight discrepancies at the initial state of the 2nd deformation stage due to unit cell offset between rhombic honeycomb layers. The influence of geometric parameters on the compressive properties such as initial peak force, mean crushing force for both stages of deformation, has been investigated.

Different to common cellular structures, the relative density and wall thickness are not the sole governing parameters for the compressive properties of the structure. Other geometric parameters such as a, b, α, and θ_0 affect the compressive response of the structure predominantly. The initial peak force of the 1st stage is mostly governed by the angles of α, and θ_0, while the edge length, a, b has more influence on the mean crushing force of the 1st stage. The additional crushing force attributed by friction during the 1st stage increases significantly with the increasing number of unit column and should not be neglected, due to the increases in swept area at the interfacial edges of the structure. For the 2nd stage of deformation, the compressive properties depend on the geometric parameters as well as the number of unit column within the structure. It is found that some of the undesired characteristics such as high initial peak crushing resistance can be mitigated by proper programming of the governing geometric parameters, without reducing the mean crushing resistance. A "graded" effect of crushing response with two uniform and programmable stages can be achieved without inducing initial peak force at either stage while keeping a uniform density throughout the structure.

Acknowledgement

The authors would like to thank Dr. Jianjun Zhang from Swinburne University for the discussion on the heat-treating of the pressed specimen. The financial support from the Australian Research Council via Discovery Early Career Researcher Award (DE160101116) is acknowledged.

References

[1] J.U. Surjadi, L. Gao, H. Du, X. Li, X. Xiong, N.X. Fang, Y. Lu, Mechanical Metamaterials and Their Engineering Applications, Advanced Engineering Materials, (2019).

[2] L.J. Gibson, M.F. Ashby, Cellular solids: structure and properties, Cambridge university press, 1999.

[3] A.G. Evans, J.W. Hutchinson, N.A. Fleck, M.F. Ashby, H.N.G. Wadley, The Topological Design of Multifunctional Cellular Metals, Progress in Material Science, 46 (2001) 309-327.

[4] V.S. Deshpande, M.F. Ashby, N.A. Fleck, Foam topology bending versus stretching dominated architectures, Acta Materialia, 49 (2001) 1035-1040.

[5] M.F. Ashby, A. Evans, N.A. Fleck, L.J. Gibson, J.W. Hutchinson, H.N.G. Wadley, Metal foams: a design guide, Materials & Design, 23 (2002) 119.

[6] T. Wierzbicki, Crushing analysis of metal honeycombs, International Journal of Impact Engineering, 1 (1983) 157-174.

[7] Z. Xue, J.W. Hutchinson, Crush dynamics of square honeycomb sandwich cores, International Journal for Numerical Methods in Engineering, 65 (2006) 2221-2245.

[8] H.N. Wadley, Multifunctional periodic cellular metals, Philos Trans A Math Phys Eng Sci, 364 (2006) 31-68.

[9] J. Zhang, M. Ashby, The out-of-plane properties of honeycombs, International Journal of Mechanical Sciences, 34 (1992) 475-489.

[10] F. Côté, V.S. Deshpande, N.A. Fleck, A.G. Evans, The out-of-plane compressive behavior of metallic honeycombs, Materials Science and Engineering: A, 380 (2004) 272-280.

[11] R.M. Neville, F. Scarpa, A. Pirrera, Shape morphing Kirigami mechanical metamaterials, Sci Rep, 6 (2016) 31067.

[12] J. Zhang, G. Lu, D. Ruan, Z. Wang, Tensile behavior of an auxetic structure: Analytical modeling and finite element analysis, International Journal of Mechanical Sciences, 136 (2018) 143-154.

[13] X. Ren, R. Das, P. Tran, T.D. Ngo, Y.M. Xie, Auxetic metamaterials and structures: A review, Smart Materials and Structures, (2018).

[14] H.Y. Jeong, S.C. An, I.C. Seo, E. Lee, S. Ha, N. Kim, Y.C. Jun, 3D printing of twisting and rotational bistable structures with tuning elements, Sci Rep, 9 (2019) 324.

[15] F. Pan, Y. Li, Z. Li, J. Yang, B. Liu, Y. Chen, 3D Pixel Mechanical Metamaterials, Adv Mater, 31 (2019) e1900548.

[16] H. Fang, K.W. Wang, S. Li, Asymmetric energy barrier and mechanical diode effect from folding multi-stable stacked-origami, Extreme Mechanics Letters, 17 (2017) 7-15.

[17] H. Fang, S.A. Chu, Y. Xia, K.W. Wang, Programmable Self-Locking Origami Mechanical Metamaterials, Adv Mater, 30 (2018) e1706311.

[18] J. Zhang, G. Lu, Dynamic tensile behaviour of re-entrant honeycombs, International Journal of Impact Engineering, 139 (2020).

[19] T. Fíla, P. Koudelka, P. Zlámal, J. Falta, M. Adorna, M. Neuhäuserová, J. Luksch, O. Jiroušek, Strain Dependency of Poisson's Ratio of SLS Printed Auxetic Lattices Subjected to

Quasi‐Static and Dynamic Compressive Loading, Advanced Engineering Materials, (2019) 1900204.

[20] N. Novak, L. Krstulović-Opara, Z. Ren, M. Vesenjak, Mechanical properties of hybrid metamaterial with auxetic chiral cellular structure and silicon filler, Composite Structures, (2019).

[21] X.-T. Wang, B. Wang, X.-W. Li, L. Ma, Mechanical properties of 3D re-entrant auxetic cellular structures, International Journal of Mechanical Sciences, 131-132 (2017) 396-407.

[22] A. Remennikov, D. Kalubadanage, T. Ngo, P. Mendis, G. Alici, A. Whittaker, Development and performance evaluation of large-scale auxetic protective systems for localised impulsive loads, International Journal of Protective Structures, (2019) 204141961985808.

[23] G. Imbalzano, P. Tran, T.D. Ngo, P.V. Lee, Three-dimensional modelling of auxetic sandwich panels for localised impact resistance, Journal of Sandwich Structures and Materials, (2015).

[24] D. Xiao, X. Kang, Y. Li, W. Wu, J. Lu, G. Zhao, D. Fang, Insight into the negative Poisson's ratio effect of metallic auxetic reentrant honeycomb under dynamic compression, Materials Science and Engineering: A, 763 (2019) 138151.

[25] M. Schenk, S.D. Guest, Geometry of Miura-folded metamaterials, Proc Natl Acad Sci U S A, 110 (2013) 3276-3281.

[26] J. Zhang, D. Karagiozova, Z. You, Y. Chen, G. Lu, Quasi-static large deformation compressive behaviour of origami-based metamaterials, International Journal of Mechanical Sciences, 153 (2019) 194-207.

[27] J.M. Gattas, W. Wu, Z. You, Miura-Base Rigid Origami: Parameterizations of First-Level Derivative and Piecewise Geometries, Journal of Mechanical Design, 135 (2013) 111011-111011-111011.

[28] X. Zhou, H. Wang, Z. You, Mechanical properties of Miura-based folded cores under quasi-static loads, Thin-Walled Structures, 82 (2014) 296-310.

[29] X.M. Xiang, G. Lu, D. Ruan, Z. You, M. Zolghadr, Large deformation of an arc-Miura structure under quasi-static load, Composite Structures, 182 (2017) 209-222.

[30] Z. Li, W. Chen, H. Hao, Crushing behaviours of folded kirigami structure with square dome shape, International Journal of Impact Engineering, 115 (2018) 94-105.

[31] Z. Chen, T. Wu, G. Nian, Y. Shan, X. Liang, H. Jiang, S. Qu, Ron Resch Origami Pattern Inspired Energy Absorption Structures, Journal of Applied Mechanics, 86 (2018) 011005-011005-011007.

[32] G.V. Rodrigues, L.M. Fonseca, M.A. Savi, A. Paiva, Nonlinear dynamics of an adaptive origami-stent system, International Journal of Mechanical Sciences, 133 (2017) 303-318.

[33] D. Karagiozova, J. Zhang, G. Lu, Z. You, Dynamic in-plane compression of Miura-ori patterned metamaterials, International Journal of Impact Engineering, 129 (2019) 80-100.

[34] J. Ma, J. Song, Y. Chen, An origami-inspired structure with graded stiffness, International Journal of Mechanical Sciences, 136 (2018) 134-142.

[35] Z. Zhai, Y. Wang, H. Jiang, Origami-inspired, on-demand deployable and collapsible mechanical metamaterials with tunable stiffness, Proceedings of the National Academy of Sciences, 115 (2018) 2032-2037.

[36] E.T. Filipov, T. Tachi, G.H. Paulino, Origami tubes assembled into stiff, yet reconfigurable structures and metamaterials, Proc Natl Acad Sci U S A, 112 (2015) 12321-12326.

[37] L. de Waal, Z. You, Graded Origami Honeycomb Tube for Energy Absorption, in: International Design Engineering Technical Conferences and Computers and Information in Engineering Conference, American Society of Mechanical Engineers, 2019, pp. V05BT07A040.

[38] Y.L. He, P.W. Zhang, Z. You, Z.Q. Li, Z.H. Wang, X.F. Shu, Programming mechanical metamaterials using origami tessellations, Composites Science and Technology, 189 (2020).

[39] X. Zhang, H. Zhang, Theoretical and numerical investigation on the crush resistance of rhombic and kagome honeycombs, Composite Structures, 96 (2013) 143-152.

[40] N. Jones, Structural impact, Cambridge university press, 2011.

[41] W. Abramowicz, N. Jones, Dynamic axial crushing of square tubes, International Journal of Impact Engineering, 2 (1984) 179-208.

[42] W. Abramowicz, N. Jones, Dynamic progressive buckling of circular and square tubes, International Journal of Impact Engineering, 4 (1986) 243-270.

[43] W. Abramowicz, N. Jones, Transition from initial global bending to progressive buckling of tubes loaded statically and dynamically, International Journal of Impact Engineering, 19 (1997) 415-437.

[44] W. Abramowicz, T. Wierzbicki, Axial Crushing of Multicorner Sheet Metal Columns, Journal of Applied Mechanics, 56 (1989) 113-120.

[45] W. Chen, T. Wierzbicki, Relative merits of single-cell, multi-cell and foam-filled thin-walled structures in energy absorption, Thin-Walled Structures, 39 (2001) 287-306.

[46] X. Zhang, G. Cheng, A comparative study of energy absorption characteristics of foam-filled and multi-cell square columns, International Journal of Impact Engineering, 34 (2007) 1739-1752.

[47] A. Najafi, M. Rais-Rohani, Mechanics of axial plastic collapse in multi-cell, multi-corner crush tubes, Thin-Walled Structures, 49 (2011) 1-12.

[48] J.M. Gattas, Z. You, Quasi-static impact of indented foldcores, International Journal of Impact Engineering, 73 (2014) 15-29.

[49] R.K. Fathers, J.M. Gattas, Z. You, Quasi-static crushing of eggbox, cube, and modified cube foldcore sandwich structures, International Journal of Mechanical Sciences, 101-102 (2015) 421-428.

[50] G. Lu, T. Yu, Energy Absorption of Structures and Materials, Woodhead publishing limited, Cambridge England, 2003.

[51] F. Côté, V.S. Deshpande, N.A. Fleck, A.G. Evans, The compressive and shear responses of corrugated and diamond lattice materials, International Journal of Solids and Structures, 43 (2006) 6220-6242.

[52] D. Ruan, G. Lu, F. Chen, E. Siores, Compressive behaviour of aluminium foams at low and medium strain rates, Composite Structures, 57 (2002) 331-336.

[53] G.M. Nagel, D.P. Thambiratnam, Computer simulation and energy absorption of tapered thin-walled rectangular tubes, Thin-Walled Structures, 43 (2005) 1225-1242.